

# Efficiency Potential and Voltage Loss of Inorganic CsPbI<sub>2</sub>Br Perovskite Solar Cells

Max Grischek,\* Pietro Caprioglio, Jiahuan Zhang, Francisco Peña-Camargo, Kári Sveinbjörnsson, Fengshuo Zu, Dorothee Menzel, Jonathan H. Warby, Jinzhao Li, Norbert Koch, Eva Unger, Lars Korte, Dieter Neher, Martin Stolterfoht,\* and Steve Albrecht\*

Inorganic perovskite solar cells show excellent thermal stability, but the reported power conversion efficiencies are still lower than for organic–inorganic perovskites. This is mainly caused by lower open-circuit voltages ( $V_{OC}$ s). Herein, the reasons for the low  $V_{OC}$  in inorganic CsPbI<sub>2</sub>Br perovskite solar cells are investigated. Intensity-dependent photoluminescence measurements for different layer stacks reveal that n–i–p and p–i–n CsPbI<sub>2</sub>Br solar cells exhibit a strong mismatch between quasi-Fermi level splitting (QFLS) and  $V_{OC}$ . Specifically, the CsPbI<sub>2</sub>Br p–i–n perovskite solar cell has a QFLS– $e \cdot V_{OC}$  mismatch of 179 meV, compared with 11 meV for a reference cell with an organic–inorganic perovskite of similar bandgap. On the other hand, this study shows that the CsPbI<sub>2</sub>Br films with a bandgap of 1.9 eV have a very low defect density, resulting in an efficiency potential of 20.3% with a MeO–2PACz hole-transporting layer and 20.8% on compact TiO<sub>2</sub>. Using ultraviolet photoelectron spectroscopy measurements, energy level misalignment is identified as a possible reason for the QFLS– $e \cdot V_{OC}$  mismatch and strategies for overcoming this  $V_{OC}$  limitation are discussed. This work highlights the need to control the interfacial energetics in inorganic perovskite solar cells, but also gives promise for high efficiencies once this issue is resolved.

length,<sup>[2,3]</sup> and a tunable band gap<sup>[4]</sup> enabled a published record efficiency of 25.7%,<sup>[5]</sup> that is close to best PCEs of silicon solar cells. To further increase the efficiency, perovskite and silicon can be combined in a tandem solar cell. In such a tandem solar cell, the perovskite and silicon subcells absorb different parts of the solar spectrum due to their different bandgaps. This leads to broader absorption as compared with perovskite single-junction solar cells and to decreased thermalization losses as compared with silicon single-junction solar cells, enabling a best published efficiency of 29.15%.<sup>[6]</sup>


One prerequisite for successful commercialization of a photovoltaic technology is the long-term stability of the solar cell. A solar cell has to withstand humidity, shading, mechanical stress, and high temperatures both during operation and fabrication. At temperatures of 150 °C and above, organic–inorganic perovskites

become unstable.<sup>[7]</sup> However, temperatures of 140–160 °C are generally used in lamination processes for solar cell encapsulation.<sup>[8]</sup> This instability is caused by lead halides with organic cations such as methylammonium (MA<sup>+</sup>) and formamidinium (FA<sup>+</sup>) decomposing to volatile products.<sup>[9]</sup> Inorganic cations such as Cs<sup>+</sup> are not volatile at these temperatures. Replacing the

## 1. Introduction

Perovskite solar cells are one of the most promising technologies to further decrease the cost of solar energy conversion. The exceptional material properties of lead halide perovskites such as a high absorption coefficient,<sup>[1]</sup> a long charge carrier diffusion

M. Grischek, J. Zhang, K. Sveinbjörnsson, D. Menzel, L. Korte, S. Albrecht  
Department Perovskite Tandem Solar Cells  
Helmholtz-Zentrum Berlin  
12489 Berlin, Germany  
E-mail: max.grischek@helmholtz-berlin.de;  
steve.albrecht@helmholtz-berlin.de

 The ORCID identification number(s) for the author(s) of this article can be found under <https://doi.org/10.1002/solr.202200690>.

<sup>[†]</sup>Present address: Clarendon Laboratory, University of Oxford, Parks Road, Oxford OX1 3PU, UK

© 2022 The Authors. Solar RRL published by Wiley-VCH GmbH. This is an open access article under the terms of the Creative Commons Attribution License, which permits use, distribution and reproduction in any medium, provided the original work is properly cited.

DOI: 10.1002/solr.202200690

M. Grischek, P. Caprioglio,<sup>[†]</sup> F. Peña-Camargo, J. H. Warby, D. Neher, M. Stolterfoht  
Institute of Physics and Astronomy  
University of Potsdam  
14476 Potsdam, Germany  
E-mail: stolterf@uni-potsdam.de

F. Zu, N. Koch  
Institut für Physik & IRIS Adlershof  
Humboldt-Universität zu Berlin  
12489 Berlin, Germany

J. Li, E. Unger  
Department Solution Processing of Hybrid Materials & Devices  
Helmholtz-Zentrum Berlin  
12489 Berlin, Germany

organic cations in the perovskite material with  $\text{Cs}^+$  has been shown to improve the solar cell stability under illumination as well as at temperatures of  $70^\circ\text{C}$ .<sup>[9]</sup>

$\text{CsPbX}_3$  ( $X = \text{Cl}, \text{Br}$  or  $\text{I}$ ) solar cells have been demonstrated and a power conversion efficiency (PCE) of 21% has been reached using  $\text{CsPbI}_3$ .<sup>[10]</sup> However, the photoactive phase of pure  $\text{CsPbI}_3$  is thermodynamically unstable at room temperature.<sup>[11]</sup> In contrast, compositions with iodide and bromide such as  $\text{CsPbI}_2\text{Br}$  exhibit a stable photoactive phase at room temperature and at a relative humidity of 30%.<sup>[12]</sup> Recently,  $\text{CsPbI}_2\text{Br}$  solar cells with a record PCE of 17.51%<sup>[13]</sup> have been reported. Their large bandgap of 1.9 eV makes them suitable for triple-junction tandem solar cells, which require a broader-bandgap top cell than tandem solar cells. In addition, the large bandgap enables high open-circuit voltages ( $V_{\text{OC}}$ ) which are needed, for example, for power generation under weak illumination<sup>[14]</sup> and for catalytic devices.<sup>[15]</sup>

To compare inorganic perovskites with their organic-inorganic counterparts, we summarize the voltage loss for solar cells with different bandgaps in **Figure 1**. We define the voltage loss as  $E_{\text{G}} - e \cdot V_{\text{OC}}$ , where  $E_{\text{G}}$  is the bandgap energy of the material,  $e$  is the elementary charge, and  $V_{\text{OC}}$  is the measured open-circuit voltage of the solar cell. For all compositions depicted, the voltage loss in inorganic perovskite solar cells is significantly higher than in organic-inorganic perovskite solar cells. Understanding, and consequently reducing, the voltage loss is therefore essential for further improvements in the field of inorganic perovskite solar cells.

Voltage loss can be caused by various layers or interfaces in a solar cell. Perovskite solar cells typically consist of a perovskite absorber, two charge transport layers (CTLs), and two electrodes, i.e. a metal electrode and a transparent conductive oxide (TCO) on a glass substrate. The hole-selective CTL, also referred to as hole-transporting layer (HTL), is more conductive for holes and the electron-transporting layer (ETL) is more conductive for

electrons. A solar cell with the HTL or ETL on the glass/TCO substrate is referred to as p-i-n or n-i-p solar cell, respectively.

In order to reveal the contribution of each CTL to the voltage loss, photoluminescence (PL) measurements are often used to quantify the internal voltage or quasi-Fermi-level splitting (QFLS) of perovskite films and stacks. The quasi-Fermi levels (QFL) describe the charge carrier density for holes and electrons in nonequilibrium conditions, such as illumination or charge injection, and the difference between the quasi-Fermi levels is called QFLS. In optimized solar cells, the QFLS can be equal to  $e \cdot V_{\text{OC}}$ . In most solar cells however, a mismatch remains between QFLS and  $e \cdot V_{\text{OC}}$ .

This QFLS- $e \cdot V_{\text{OC}}$  mismatch is related to the fact that the QFLS measured with PL is determined by different recombination pathways. For various organic-inorganic perovskites, we have recently shown that the QFLS is mostly limited by interface recombination at the CTLs, rather than in the perovskite's bulk.<sup>[16]</sup> A large QFLS- $e \cdot V_{\text{OC}}$  mismatch has been mostly attributed to energy offsets at the perovskite/CTL interface, which cause a bending of the QFL. This bending of QFL primarily reduces the  $V_{\text{OC}}$ , rather than the QFLS.<sup>[17]</sup> This has been shown experimentally for a  $\text{Cs}_{0.05}(\text{FA}_{0.83}\text{MA}_{0.17})_{0.95}\text{Pb}(\text{I}_{0.83}\text{Br}_{0.17})_3$  triple-cation perovskite where the HTLs PEDOT:PSS and P3HT were compared with PTAA:PFN. As a result, the decrease in the QFLS was observed to be much lower than the respective decrease in  $V_{\text{OC}}$ .<sup>[18]</sup> The mismatch between the QFLS and the final device  $V_{\text{OC}}$  is usually very small for thoroughly optimized organic-inorganic perovskite solar cells. However, this QFLS- $e \cdot V_{\text{OC}}$  mismatch might represent a large contribution to the voltage loss and is therefore of high importance, especially in less-investigated and therefore less-optimized perovskite solar cells.

The majority and minority QFL must collapse and meet at the electrode as a metal cannot support a QFLS. It is established knowledge that the QFLS- $e \cdot V_{\text{OC}}$  mismatch depends on the relative bending of the majority and minority QFL in the contact region as they collapse toward the electrode. The relative bending depends on the conductivities of the carriers in the region of interest. This can be expressed as in Equation (1), as stated by Onno et al.,<sup>[17]</sup> which is based on the work by Würfel et al.,<sup>[19]</sup> here shown for an HTL.

$$\frac{e \cdot V_{\text{OC}}}{\text{QFLS}} = \frac{\rho_{c,e}}{\rho_{c,e} + \rho_{c,h}} \quad (1)$$

Here,  $e$  is the elementary charge and  $\rho_{c,e}$  and  $\rho_{c,h}$  are the injection-dependent partial specific contact resistances for electrons and holes, respectively.

Therefore, to achieve a low QFLS- $e \cdot V_{\text{OC}}$  mismatch, the specific contact resistance of the majority carrier (e.g., holes) in the (e.g., hole-selective) CTL or at the critical interface needs to be low. This means that the conductivity for these majority carriers needs to be large. This can be achieved by aligning the electrode work function with the conduction or valence band of the absorber layer for the case of well-aligned CTLs and using doped transport layers. Therefore, the QFLS- $e \cdot V_{\text{OC}}$  mismatch can be caused by an interlayer with low conductivity for the charge type to be conducted and/or by misaligned energy levels of the CTLs and/or of the electrode.<sup>[20]</sup> In general, the underlying reason for the QFLS- $e \cdot V_{\text{OC}}$  mismatch in a specific solar cell is

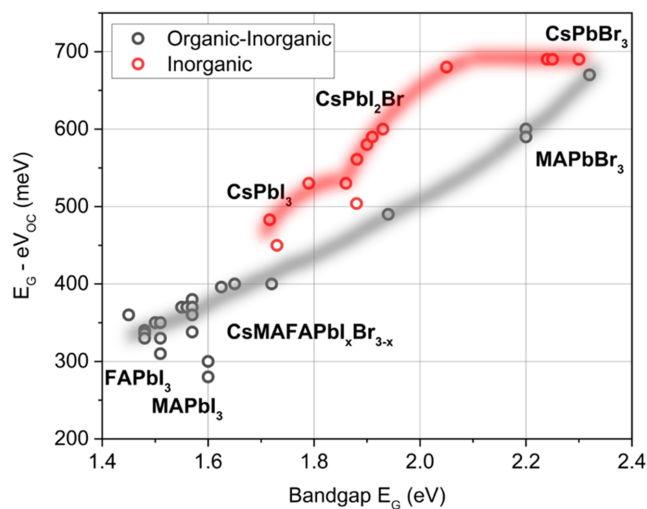


**Figure 1.** Selected voltage loss ( $E_{\text{G}} - e \cdot V_{\text{OC}}$ ) values for various organic-inorganic and inorganic perovskite solar cells based on record  $V_{\text{OC}}$ s for different bandgaps collected from Perovskite Database<sup>[42]</sup> and studies.<sup>[43–46]</sup> The different compositions are indicated and lines are included as visual guides.

often hard to identify and more experiments are needed to investigate the origin of this important voltage loss mechanism.

As the  $QFLS-e \cdot V_{OC}$  mismatch strongly depends on the absorber and CTL combination, it is important to focus on the contact materials used for inorganic perovskites. The majority of published reports on  $CsPbI_2Br$  perovskite compositions have used  $n-i-p$  device architectures with  $TiO_2$ ,  $SnO_2$ , or  $ZnO$  as ETL and spiro-OMeTAD, PTAA, or P3HT as HTL.<sup>[21]</sup> The metal oxide ETLs typically need annealing temperatures above 200 °C. In the long run, inorganic perovskites might be integrated as top cells into tandem solar cell devices with temperature-sensitive bottom cells. This is why other CTLs have to be tested, for example, in  $p-i-n$  device architecture.

In this work, we investigate both  $p-i-n$  and  $n-i-p$   $CsPbI_2Br$  perovskite solar cells to analyze the efficiency potential and the losses caused by each layer. We develop a fabrication process for  $CsPbI_2Br$  that uses a low annealing temperature of 160 °C. This enables us to use an HTL formed by the self-assembling molecule [2-(3,6-Dimethoxy-9H-carbazol-9-yl)ethyl]phosphonic Acid (MeO-2PACz) for the first time in a  $p-i-n$   $CsPbI_2Br$  solar cell. The structure diagram of MeO-2PACz is shown in Figure S16, Supporting Information. A self-assembled monolayer such as MeO-2PACz achieves a very low thickness of one monolayer with complete coverage of the sample.<sup>[22]</sup> This leads to substantially higher fill factors (FF) as compared with other HTLs such as PTAA.<sup>[23]</sup> We fabricate perovskite films on various CTLs and measure their radiative efficiency potential using intensity-dependent PL. With that, we identify the voltage loss and therefore the most promising CTLs for inorganic perovskite solar cells. In a second step, we fabricate  $p-i-n$  and  $n-i-p$  solar cells and quantify the efficiency potential of the perovskite by adding one layer at a time.

With this layer-by-layer loss analysis, we reveal the contribution of each interface to the voltage loss. In the  $n-i-p$   $CsPbI_2Br$  solar cells, losses in QFLS are caused in almost equal parts by ETL and HTL. In the  $p-i-n$  solar cells, the main part of the QFLS losses is caused by the ETL alone. We further find that both  $p-i-n$  and  $n-i-p$  solar cells have a high efficiency potential due to high measured QFLS and high potential FF (pFF). However, the  $V_{OC}$  of the device is substantially lower than the QFLS. This  $QFLS-e \cdot V_{OC}$  mismatch is most pronounced in  $p-i-n$  solar cells with a difference of 178 meV. Therefore, we further compare the voltage losses of inorganic  $p-i-n$  solar cells with an organic-inorganic perovskite solar cell with the composition  $Cs_{0.05}(FA_{0.5}MA_{0.5})_{0.95}Pb_{(10.5}Br_{0.5})_3$  and examine possible reasons for the  $QFLS-e \cdot V_{OC}$  mismatch. This comparison reveals that the organic-inorganic perovskite solar cell exhibits a  $QFLS-e \cdot V_{OC}$  mismatch of only 10 meV, although the perovskite bandgap is the same and similar CTLs have been used. Finally, we investigate the energy-level alignment in  $p-i-n$   $CsPbI_2Br$  solar cells using ultraviolet and X-ray photoelectron spectroscopy (UPS and XPS) measurements. With this, we identify energy-level misalignment as a possible reason for the large  $QFLS-e \cdot V_{OC}$  mismatch.

## 2. Results

Inorganic perovskite solar cells are mainly fabricated either in nitrogen or in clean dry air (CDA) atmosphere. We found that

a combination of the two yielded the best results. In the fabrication process we developed, we first spin coated a stoichiometric  $CsPbI_2Br$  solution in DMSO in a nitrogen-filled glove box. After spin coating, we let the films rest in the nitrogen-filled glove box for 30 min before transferring them to a glove box filled with CDA for annealing at 160 °C for 10 min. While spin coating in nitrogen atmosphere led to a more reproducible process, annealing in dry air led to higher solar cell performance than annealing in nitrogen, as shown in Figure S1 and S2, Supporting Information. This improved performance has previously been reported to be caused by oxygen atoms passivating halide vacancies in the perovskite crystal structure during annealing.<sup>[24]</sup>

The CTL on top of the glass/TCO substrate greatly influences the perovskite film and interface properties, as it affects the growth of the perovskite. To identify the most promising bottom CTL, that is, the CTL on top of which the perovskite is spin coated, we performed intensity-dependent PL measurements. This measurement technique was first used for perovskite solar cells by Sarritzu et al.<sup>[25]</sup> We recently used this method to identify contact layer-mediated losses for organic-inorganic perovskites.<sup>[16]</sup> Other reports have used this technique to compare the efficiency potential of  $Cs_{0.05}(FA_{0.77}MA_{0.23})_{0.95}Pb(I_{0.77}Br_{0.23})_3$  perovskite on various HTLs<sup>[23]</sup> and to quantify the efficiency potential of silicon-perovskite tandem solar cells and their sub cells.<sup>[26]</sup>

We determined the bandgap of the  $CsPbI_2Br$  perovskite to be 1.896 eV by measuring the external quantum efficiency (EQE) of a  $CsPbI_2Br$  perovskite solar cell and finding the maximum of the first derivative  $\partial(EQE)/\partial\lambda$  shown in Figure S3, Supporting Information, as proposed by Almora et al.<sup>[27]</sup> Bromide-rich organic-inorganic perovskites show halide segregation under illumination, which shifts the PL emission peak and changes the PL quantum yield (PLQY).<sup>[28]</sup> Here, the PL peak position remains unchanged over a time of 5 min, as shown in Figure S4, Supporting Information. This excludes halide segregation in  $CsPbI_2Br$  perovskite films. In addition, all studied films are free from pinholes, as seen in top-view images from scanning electron microscopy in Figure S7, Supporting Information. An SEM image of a cross section of a perovskite film on MeO-2PACz shows differences in film thickness horizontally but a relatively smooth surface at the broken edge; see Figure S8, Supporting Information. This perovskite film quality is a prerequisite for the successful use in solar cells.

Figure 2a shows the samples we studied: namely,  $CsPbI_2Br$  films on glass, on glass with an indium-doped tin oxide (ITO) coating, on the HTLs MeO-2PACz and P3CT-N and on the ETLs tin oxide ( $SnO_2$ ), compact titanium dioxide ( $TiO_2$ ), and a double layer consisting of compact and mesoporous  $TiO_2$ . P3CT-N was synthesized through the reaction of poly[3-(4-carboxylbutyl)thiophene (P3CT) with methylamine ( $CH_3NH_2$ ).<sup>[29]</sup> The illumination intensity of the excitation used for PL measurements was calibrated by measuring the photocurrent of a solar cell and varying the intensity until the photocurrent reached the value measured under illumination corresponding to the AM 1.5G standard solar spectrum, that is, 1 sun equivalent. Figure 2b shows PL spectra recorded at different illumination intensities ranging from 0.001 to 4 sun equivalents. The PL spectra for  $CsPbI_2Br$  on glass reveal

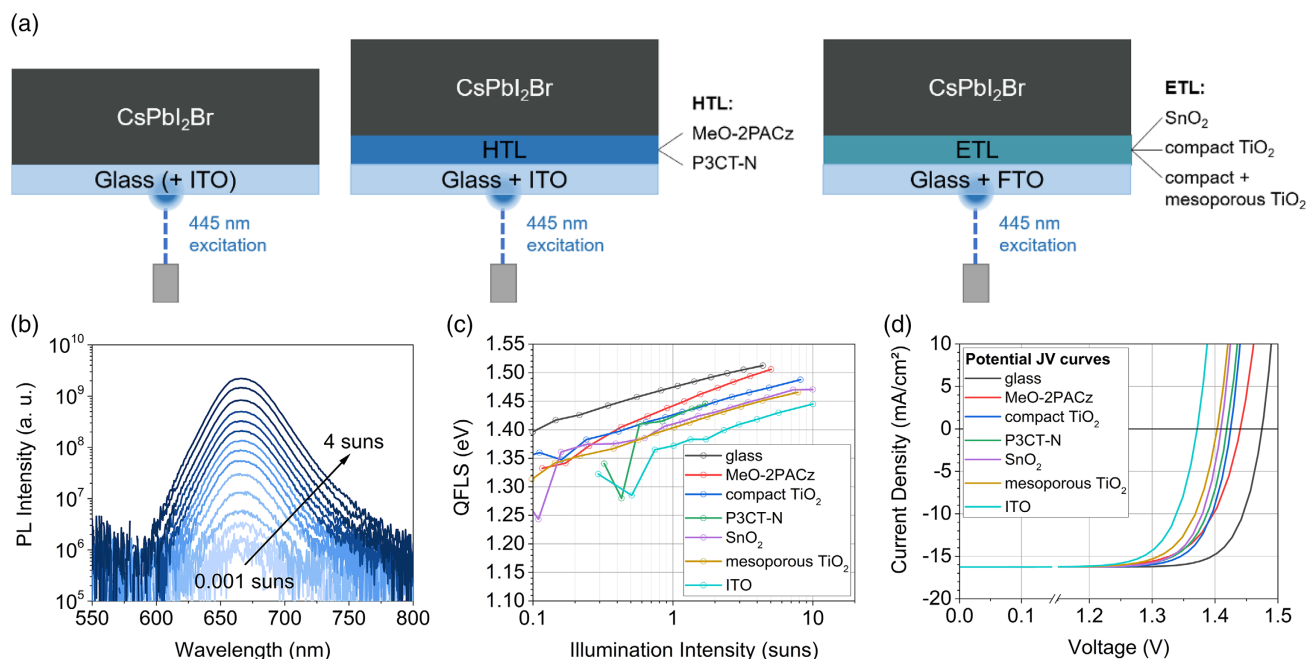


**Figure 2.** a) Samples studied with PL measurements: CsPbI<sub>2</sub>Br films on glass, on glass with indium tin oxide (ITO) coating, on the hole-transporting layer (HTL) MeO-2PACz, and on various electron-transporting layers (ETLs). b) Absolute PL spectra for various illumination intensities for CsPbI<sub>2</sub>Br on ITO. c) QFLS extracted from the PL spectra for various illumination intensities for CsPbI<sub>2</sub>Br films on glass and glass/ITO as well as different CTLs. The ideality factor ( $n_{ID}$ ) values extracted from fits of the data are 1.2 for the CsPbI<sub>2</sub>Br film on glass, compact TiO<sub>2</sub>, and SnO<sub>2</sub>, 1.3 on ITO and P3CT-N, 1.4 on mesoporous TiO<sub>2</sub>, and 1.7 on MeO-2PACz. d) Potential current density–voltage ( $pJ$ – $V$ ) curves extracted from fits of the data shown in panel (b) by assuming an EQE of 95% as described in the text.

a PL quantum yield (PLQY) of 1.39% under 1 sun equivalent illumination. For comparison, organic–inorganic perovskite films on glass that we measured in a previous study showed PLQY of up to 1% for various compositions, but also an exceptionally high PLQY of 27.7% on Cs<sub>0.06</sub>FA<sub>0.79</sub>MA<sub>0.15</sub>Pb(I<sub>0.85</sub>Br<sub>0.15</sub>)<sub>3</sub> films with potassium passivation as previously shown by Abdi-Jalebi et al.<sup>[30]</sup>

For each absolute PL spectrum, we calculated the QFLS according to the method presented in our previous study.<sup>[16]</sup> The results for QFLS versus intensity are shown in Figure 2c for the samples presented in Figure 2a. Perovskite on glass yields the highest QFLS with 1.474 eV and the QFLS were substantially reduced by the introduction of CTLs. MeO-2PACz/perovskite yields a high QFLS of 1.441 eV, P3CT-N shows a QFLS of 1.42 eV, and the ETL/perovskite stacks show QFLS values from

1.372 to 1.425 eV with the highest value for compact TiO<sub>2</sub>, as shown in Table 1.

The QFLS represents the internal voltage multiplied by the elementary charge  $e$  and is caused by the illumination. The illumination intensity is directly proportional to the generated current density in the absorber material.<sup>[16]</sup> Therefore, by converting the illumination intensity to the respective current density in the solar cell as described above and by shifting the potential current density–voltage ( $pJ$ – $V$ ) curves by the potential short-circuit current density ( $pJ_{SC}$ ), suns–QFLS curves can be converted to potential  $J$ – $V$  curves. These  $pJ$ – $V$  curves are shown in Figure 2d and do not only show the potential open-circuit voltage ( $pV_{OC}$ ) and short-circuit current density ( $pJ_{SC}$ ), but also the potential FF ( $pFF$ ) of the measured film stack without the need for complete solar cells. We calculated the potential  $J_{SC}$  from the bandgap of the

**Table 1.** Performance parameters from potential  $J$ – $V$  curves of CsPbI<sub>2</sub>Br perovskite films on different CTLs shown in Figure 2c and the resulting efficiency potential ( $pPCE$ ), the measured ideality factor ( $n_{ID}$ ), as well as PLQY.

CTL	$pFF$ [%]	$pV_{OC}$ [V]	$pJ_{SC}$ [mA cm <sup>-2</sup> ]	$pPCE$ [%]	$n_{ID}$	PLQY [%]
glass	90.0	1.474	16.26	21.6	1.2	1.390
MeO-2PACz	86.6	1.441	16.26	20.3	1.7	0.367
compact TiO <sub>2</sub>	89.6	1.425	16.26	20.8	1.2	0.203
P3CT-N	89.0	1.42	16.26	20.5	1.3	0.164
SnO <sub>2</sub>	89.6	1.409	16.26	20.5	1.2	0.112
mesop. TiO <sub>2</sub> + LiTFSI	88.2	1.404	16.26	20.1	1.4	0.088
ITO	88.7	1.372	16.26	19.8	1.3	0.026

perovskite assuming an EQE of 95%. The resulting potential  $J_{SC}$  is  $16.26 \text{ mA cm}^{-2}$ . We consider this potential  $J_{SC}$  as the maximum achievable value for state-of-the-art perovskite solar cells, as an average EQE of 95% has been certified for n-i-p solar cells.<sup>[31]</sup>

The radiative ideality factor ( $n_{ID}$ ) is a measure for the amount of nonradiative recombination and can be determined from the slope of the QFLS against intensity. Interestingly, all the perovskite samples show low ideality factors of 1.0–1.3, except for mesoporous  $\text{TiO}_2$  (1.4) and MeO-2PACz (1.7). These low ideality factors cause exceptionally high potential FF of around 90%. This results in potential efficiencies of 21.6% for the neat perovskite, 20.1–20.8% for the ETLs, and 20.3% and 20.5% for the HTLs. These values are considerably higher than the highest published PCE of 17.51% for  $\text{CsPbI}_2\text{Br}$  solar cells.<sup>[13]</sup>

Based on these PL results, compact  $\text{TiO}_2$  and P3CT-N are the most promising ETL and HTL, respectively, for  $\text{CsPbI}_2\text{Br}$  solar cells. The HTL MeO-2PACz shows the highest  $pV_{OC}$  of all CTLs, which is only 33 meV lower than on glass. The  $pV_{OC}$  on compact  $\text{TiO}_2$  is only 49 meV lower than on glass and the  $pV_{OC}$  on P3CT-N is only 54 meV lower than on glass. This indicates a low defect density derived from our radiative measurements at the CTL/ $\text{CsPbI}_2\text{Br}$  interface for these three CTLs. The pFF of the films on compact  $\text{TiO}_2$  and P3CT-N are on par with that on glass, while the pFF on MeO-2PACz is slightly lower than on glass.

Different CTLs can lead to differences in the crystallinity of  $\text{CsPbI}_2\text{Br}$ , which can influence the PLQY. To investigate differences in crystallinity, we measured X-ray diffraction (XRD) patterns of  $\text{CsPbI}_2\text{Br}$  films on glass and on MeO-2PACz. Despite visual changes in microscopic images, no substantial differences were observed in the XRD patterns despite the preferential orientation; see Figure S5, Supporting Information.

So far, we investigated the efficiency potentials of half cells comprising only one electrode and one CTL, that is, the transparent conductive oxide (TCO) such as ITO or FTO and one CTL such as MeO-2PACz or metal oxides. For a thorough and relevant loss analysis, complete solar cells with all necessary CTLs and electrodes are required. Therefore, we fabricated complete solar cells in p-i-n and n-i-p configuration using the CTLs presented in Table 1. We focus on the best-performing solar cells which for the n-i-p configuration in this study employed a mesoporous  $\text{TiO}_2$  on top of a compact  $\text{TiO}_2$  as ETL. Solar cells using this ETL performed better than those using only compact  $\text{TiO}_2$ , as shown in Figure S6, Supporting Information. We spin coated a lithium bis (tri-fluoromethanesulfonyl) imide (LiTFSI) solution on top of the mesoporous  $\text{TiO}_2$  followed by annealing to evaporate the solvent and sintering at  $450^\circ\text{C}$  for 30 min. This has been reported to enhance the electron extraction of the mesoporous  $\text{TiO}_2$ .<sup>[32]</sup> We used spiro-OMeTAD as the HTL and Au as the metal electrode. A schematic diagram of the complete device stack is shown in Figure 3a.

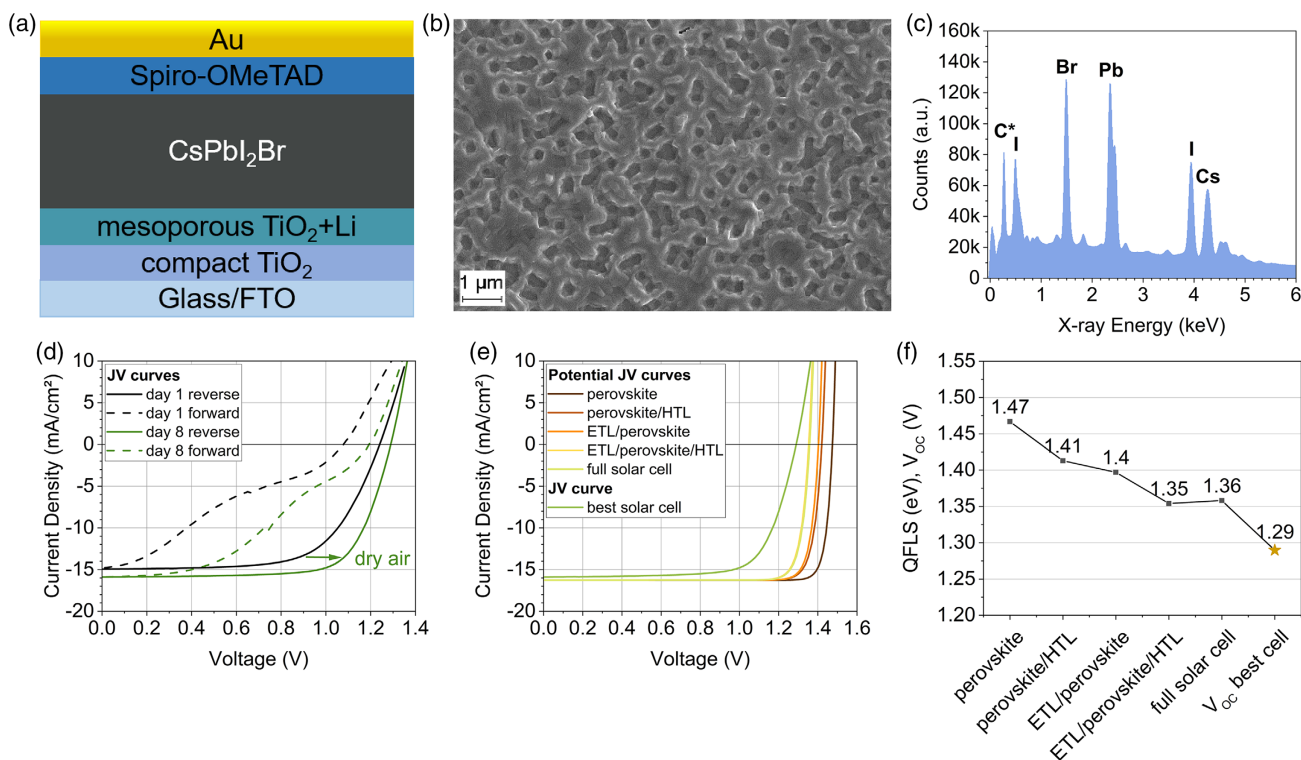


**Figure 3.** a) Layer stack of n-i-p solar cells analyzed in this work. b) Top-view SEM image of  $\text{CsPbI}_2\text{Br}$  film on compact and mesoporous  $\text{TiO}_2$  doped with Li. c) EDS signals for detected elements in  $\text{CsPbI}_2\text{Br}$  films on mesoporous  $\text{TiO}_2$  obtained with an EHT of 10 kV. Note that the detected carbon peak most likely originates from surface impurities and/or organic contaminations from within the SEM chamber. d)  $J$ - $V$  curves for best n-i-p solar cell after 1 night in dry air glove box (day 1) and after 8 nights in dry air glove box (day 8). e) Potential  $J$ - $V$  curves from intensity-dependent QFLS measurements for different layer stacks and reverse  $J$ - $V$  curve of best n-i-p solar cell (day 8). f) Mean QFLS values (average from 2–3 samples) measured for different layer stacks as in panel (e) and  $V_{OC}$  of best n-i-p solar cell taken from the reverse scan on day 8.

The fabrication process developed for this study resulted in dense, pinhole-free films with a honeycomb-like structure on the surface; see Figure 3b. We attribute this structure to a different growth on the mesoporous TiO<sub>2</sub>, as they are not observed on any compact CTL; see Figure S7, Supporting Information. To demonstrate the inorganic nature of the perovskite, we applied energy-dispersive X-ray spectroscopy (EDS) of the perovskite deposited on different transport layers. The signals for detected elements in CsPbI<sub>2</sub>Br perovskite films on mesoporous TiO<sub>2</sub> are shown in Figure 3c. Generally, organic–inorganic perovskites contain considerable amounts of nitrogen originating from the organic cations of the material. Nitrogen has a characteristic K $\alpha$  X-ray emission at 0.392 keV and is easily detected by EDS employing a windowless detector, see Figure S9, Supporting Information. In the case of our CsPbI<sub>2</sub>Br perovskite film, the nitrogen emission peak is not observed, see Figure S9, Supporting Information. This indicates that there are negligible amounts of organic moieties in the perovskite film or, if there are any, that they are below the detection limits of EDS. The resulting elemental distribution of the inorganic components shows a stoichiometric CsPbI<sub>2</sub>Br composition with a slight excess of Cs on all CTLs, see Table S1, Supporting Information. The K $\alpha$  carbon peak, which is measured at 0.277 keV, can most likely be attributed to surface impurities and/or organic contaminations within the SEM chamber and is commonly detected even for purely inorganic materials such as TCOs, see Figure S9, Supporting Information.

Figure 3d shows  $J$ – $V$  curves measured under simulated AM1.5G illumination conditions, comparing the best n–i–p solar cell one day after fabrication and after seven days stored in dry air. After storage in dry air, the reverse-scan PCE increased from 12.03% to 14.90%, with a high  $V_{OC}$  of 1.29 V, a FF of 72.7%, and a  $J_{SC}$  of 15.89 mA cm<sup>-2</sup>, see Table 2. This shows that the CsPbI<sub>2</sub>Br solar cells produced in this study are stable in dry air and that the FF,  $J_{SC}$ , and  $V_{OC}$  are even increased when

**Table 2.** Performance parameters of n–i–p solar cells shown in Figure 3b extracted from  $J$ – $V$  curves under AM 1.5G illumination measured in reverse- (from  $V_{OC}$  to  $J_{SC}$ ) and forward-scanning (from  $J_{SC}$  to  $V_{OC}$ ) direction.

	FF [%]	$V_{OC}$ [V]	$J_{SC}$ [mA cm <sup>-2</sup> ]	PCE [%]
day 8 reverse	72.7	1.290	15.89	14.90
day 8 forward	40.7	1.193	15.87	7.71
day 1 reverse	64.9	1.240	14.95	12.03
day 1 forward	24.5	1.078	14.80	3.90

**Table 3.** Potential performance parameters of n–i–p layer stacks extracted from PL measurements and corresponding  $pJ$ – $V$  curves shown in Figure 3e and the resulting efficiency potential (pPCE), the measured ideality factor, and PLQY.

	pFF (%)	p $V_{OC}$ [V]	p $J_{SC}$ [mA cm <sup>-2</sup> ]	pPCE [%]	$n_D$	PLQY [%]
perovskite	90.0	1.474	16.26	21.6	1.2	1.390
perovskite/HTL	87.7	1.421	16.26	20.3	1.5	0.169
ETL/perovskite	88.2	1.404	16.26	20.1	1.4	0.088
ETL/perovskite/HTL	87.3	1.353	16.26	19.2	1.5	0.013
full solar cell	87.3	1.359	16.26	19.3	1.5	0.015

measuring on day eight. In addition, the substantial hysteresis between the forward and reverse  $J$ – $V$  scans is reduced significantly by dry air storage.

To quantify the contribution to  $V_{OC}$  and FF losses, we conducted a layer-by-layer analysis of the solar cell using intensity-dependent PL measurements. The resulting potential  $J$ – $V$  curves are compared with the measured  $J$ – $V$  curve of the solar cell in Figure 3e. The resulting potential performance parameters are presented in Table 3. The pFF of the full solar cells is 87.3%, which is only 2.7% absolute units lower than the film on glass. However, the measured FF from the reverse  $J$ – $V$  scan is only 72.7%, most likely due to transport losses of photogenerated charges. The hysteresis between the forward and reverse  $J$ – $V$  scans suggests the presence of mobile ions in the perovskite. These mobile ions are likely to cause transport losses.

To compare the voltage losses, Figure 3f shows the QFLS of each stack and the device  $V_{OC}$ . Compared with the perovskite film on glass, the HTL and the ETL cause similar voltage losses, resulting in a combined voltage loss of around 110 meV when comparing the perovskite on glass to the full solar cell. This leads to a reduced pPCE of 19.3% compared with 21.6% for perovskite on glass and 20.1% on mesoporous TiO<sub>2</sub>. Intriguingly, the device  $V_{OC}$  (1.29 V) is much lower than the QFLS of the same device (1.37 eV). We discuss this large QFLS– $e \cdot V_{OC}$  mismatch in detail in the section “Origin of QFLS– $e \cdot V_{OC}$  mismatch.”

Transport losses seem to limit the FF of n–i–p CsPbI<sub>2</sub>Br solar cells and interface recombination losses at both transport layers limit the  $V_{OC}$ . Combined with a large QFLS– $e \cdot V_{OC}$  mismatch, this leads to a reverse-scan PCE of 14.9% even though the efficiency potential deduced from intensity-dependent PL of the full solar cell is 19.3%.

To get more insights into the loss analysis of CsPbI<sub>2</sub>Br solar cells with various device configurations, additional p–i–n solar cells were manufactured and optimized for this study. Almost all published p–i–n CsPbI<sub>2</sub>Br solar cells use NiO<sub>x</sub> as HTL with some exceptions using P3HT and P3CT.<sup>[21]</sup> For the first time, we produced CsPbI<sub>2</sub>Br solar cells using MeO–2PACz as HTL, see Figure 4a. Figure 4b shows an SEM image of a perovskite film on MeO–2PACz, revealing a dense and pinhole-free film. As opposed to mesoporous TiO<sub>2</sub>, no honeycomb structure can be observed on the surface. This indicates a more homogeneous perovskite crystal growth on MeO–2PACz, resulting in a smoother surface. To verify the inorganic nature of CsPbI<sub>2</sub>Br on MeO–2PACz, we performed EDS measurements. As on mesoporous TiO<sub>2</sub>, we do not detect any presence of nitrogen in the perovskite film, see Figure S9, Supporting Information. The resulting elemental distribution shows a stoichiometric

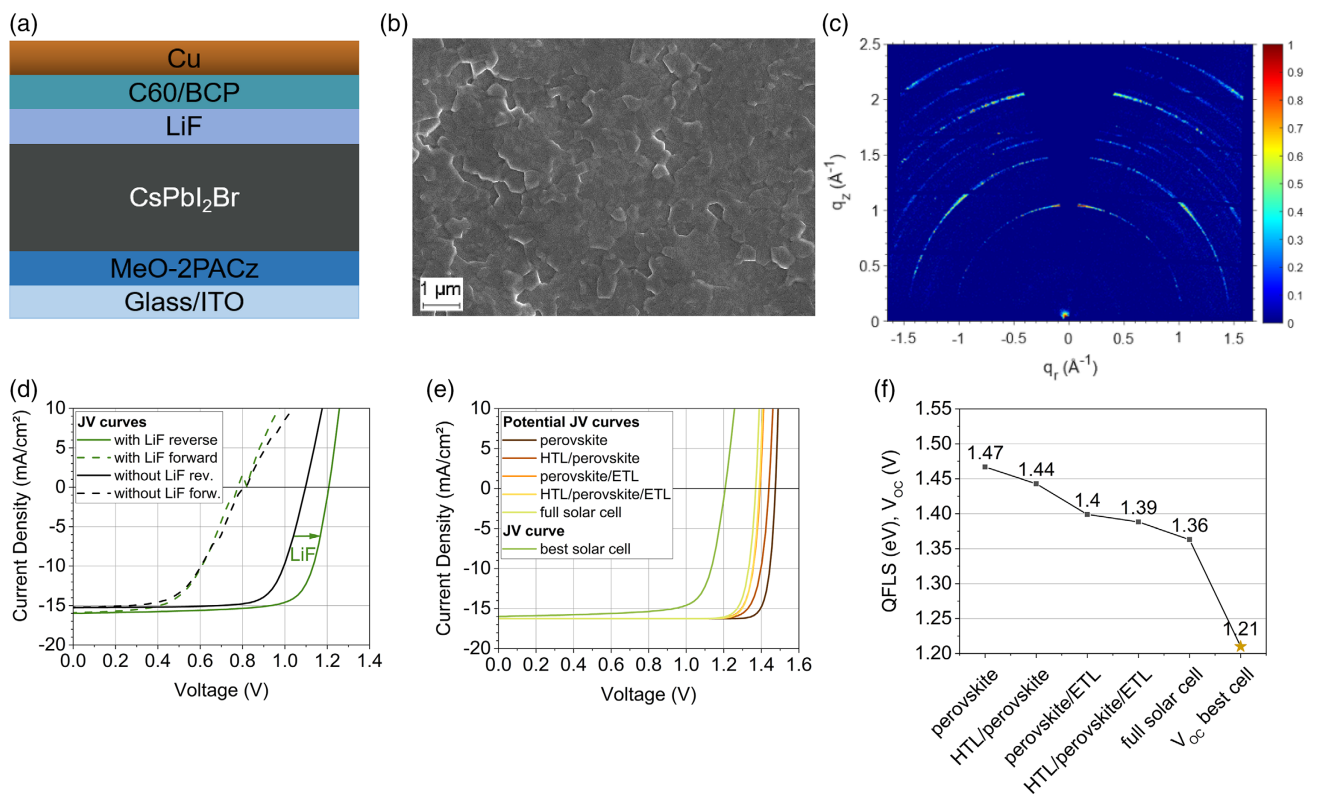


**Figure 4.** a) Layer stack of p–i–n solar cells used in this work. b) Top-view SEM image of CsPbI<sub>2</sub>Br film on MeO-2PACz. c) Synchrotron-based GIWAXS image for a CsPbI<sub>2</sub>Br film on MeO-2PACz. d) J–V curves for the best p–i–n solar cell with and without LiF between the perovskite and C<sub>60</sub>. e) Potential J–V curves from intensity-dependent PL measurements for different layer stacks and reverse J–V curve of best p–i–n solar cell (with LiF). f) Mean QFLS values (average from 2–3 samples) of the same layer stacks as in panel (e) and V<sub>oc</sub> of best p–i–n solar cell taken from the reverse J–V scan of samples with LiF.

CsPbI<sub>2</sub>Br with slight Cs excess; see Table S1, Supporting Information.

In order to investigate the quality of the CsPbI<sub>2</sub>Br crystal structure grown on MeO-2PACz, we conducted synchrotron-based grazing-incidence wide-angle X-ray scattering (GIWAXS) measurements. Figure 4c shows a GIWAXS 2D image of the CsPbI<sub>2</sub>Br film at an incidence angle of 2°. The crystals are highly oriented in out-of-plane direction, as shown by the intensity peak of the (100) plane at 90° azimuthal angle. To probe the crystallinity of bulk and surface of the films, we varied the incidence angles. Patterns for all incidence angles show the same preferential orientation, as shown in Figure S10, Supporting Information. The material shows no  $\delta$  phase both in the bulk and at the surface, as proven by the absence of a peak between 7° and 12° in Figure S11, Supporting Information. This GIWAXS data prove that a homogeneous film in pure  $\gamma$  phase can be fabricated at temperatures as low as 160 °C.<sup>[33]</sup> This is essential for perovskite deposition on temperature-sensitive CTLs or on temperature-sensitive bottom cells for tandem integration.

The J–V curves for the p–i–n CsPbI<sub>2</sub>Br solar cells are shown in Figure 4d. We measured J–V curves with and without a LiF interlayer at the interface with C<sub>60</sub>. The LiF interlayer improves the reverse scan V<sub>oc</sub> from 1.10 to 1.21 V, resulting in a PCE of 14.67%, see Table 4. The best published PCE for p–i–n CsPbI<sub>2</sub>Br solar cells is 17.46%<sup>[34]</sup> with InCl<sub>3</sub> additive and 15.4%<sup>[35]</sup> for pure CsPbI<sub>2</sub>Br. Here, a large hysteresis is observed

**Table 4.** Performance parameters of p–i–n solar cells extracted from J–V curves under AM 1.5G illumination shown in 5b measured in reverse (from V<sub>oc</sub> to J<sub>sc</sub>) and forward-scanning (from J<sub>sc</sub> to V<sub>oc</sub>) direction.

	FF [%]	V <sub>oc</sub> [V]	J <sub>sc</sub> [mA cm <sup>-2</sup> ]	PCE [%]
with LiF reverse	76.0	1.207	15.99	14.67
with LiF forward	56.0	0.777	15.93	6.93
without LiF reverse	74.9	1.097	15.26	12.54
without LiF forward	54.7	0.811	15.21	6.75

for p–i–n solar cells which is higher as compared with the n–i–p device architecture. The stabilized efficiency after 10 min of MPP tracking is 9.3% and the integrated photocurrent from EQE is 14.11 mA cm<sup>-2</sup>, as shown in Figure S12, Supporting Information. The integrated photocurrent from EQE is 1.88 mA cm<sup>-2</sup> lower than the J<sub>sc</sub> from J–V scans. This might be caused by device instability during the EQE measurement over 5–10 min or by an overestimation of the J<sub>sc</sub> due to the used scan speed. In similar perovskite solar cells, such current loss was attributed to mobile ions which accumulate at the perovskite/CTL interface, flattening the bands and decreasing charge extraction efficiency.<sup>[36]</sup> A p–i–n CsPbI<sub>2</sub>Br solar cell retained 85% of the initial PCE after MPP tracking over 10 h with an initial stabilized PCE of 10%, see Figure S12, Supporting Information.

**Table 5.** Potential performance parameters of p–i–n layer stacks from PL measurements and corresponding  $p_j$ – $V$  curves shown in Figure 4e and the resulting efficiency potential (pPCE), the measured ideality factor as well as PLQY.

	pFF [%]	pV <sub>OC</sub> [V]	p <sub>sc</sub> [mA cm <sup>-2</sup> ]	pPCE [%]	n <sub>ID</sub>	PLQY [%]
perovskite	90.0	1.474	16.26	21.6	1.2	1.390
HTL/perovskite	86.6	1.441	16.26	20.3	1.7	0.367
perovskite/ETL	87.5	1.393	16.26	19.8	1.5	0.060
HTL/perovskite/ETL	88.2	1.389	16.26	19.9	1.4	0.052
full solar cell	87.3	1.371	16.26	19.5	1.5	0.024

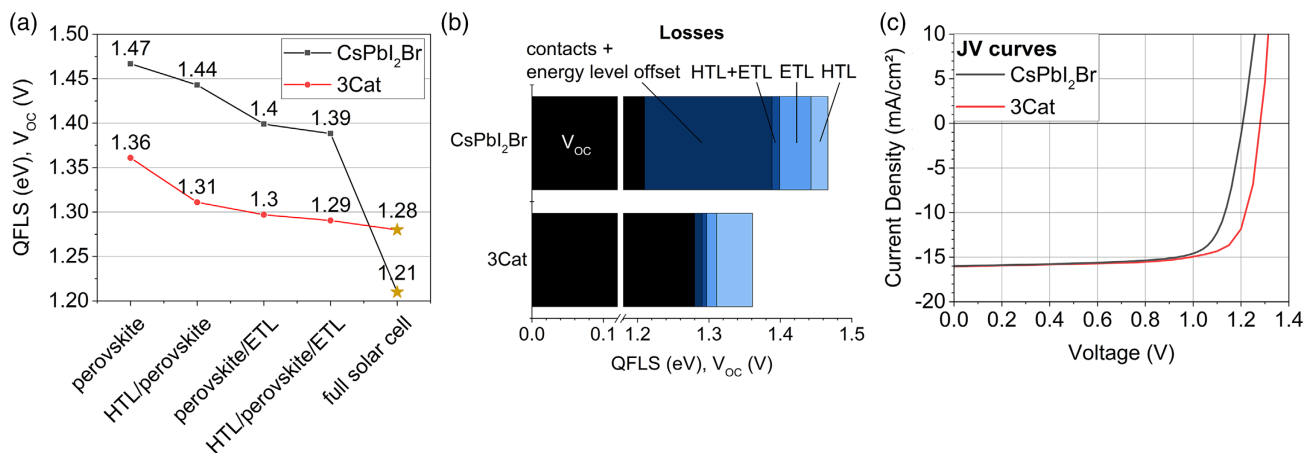
The layer-by-layer loss analysis shown in Figure 4e and **Table 5** reveals that the main part of the loss in QFLS is caused by the ETL. The MeO-2PACz/CsPbI<sub>2</sub>Br interface introduces a QFLS loss of 33 meV, while the CsPbI<sub>2</sub>Br/C<sub>60</sub> interface is responsible for QFLS losses of 81 meV. Both CTLs together induce a QFLS loss of 85 meV and a slight loss in pFF. Very interestingly, the resulting pPCE of the full p–i–n solar cell (19.5%) is even higher than for the full n–i–p solar cell (19.3%) thanks to a higher pV<sub>OC</sub>.

Figure 4f shows the average QFLS values for the different layer stacks. Intriguingly, the QFLS– $e$ ·V<sub>OC</sub> mismatch is even larger than the mismatch in n–i–p solar cells. One possible reason for the QFLS– $e$ ·V<sub>OC</sub> mismatch is recombination at a direct interface between the perovskite and the metal contact (here copper). This could be caused by inhomogeneous film formation of the 23 nm C<sub>60</sub> and 8 nm BCP in between perovskite and copper. To exclude any physical contact between the copper and the perovskite, we increased the thickness of the C<sub>60</sub> layer to 75 nm. However, the same V<sub>OC</sub> and QFLS was observed, which indicates that no direct copper–perovskite interface is formed also for thinner layers of C<sub>60</sub>. Nevertheless, we cannot exclude that the mismatch might be related to energy-level misalignment of the perovskite and the metal electrode. The unchanged V<sub>OC</sub> with 75 nm of C<sub>60</sub> also shows that the electron conductivity in the C<sub>60</sub> bulk is not responsible for the QFLS– $e$ ·V<sub>OC</sub> mismatch. However, a thicker layer of C<sub>60</sub> can still affect the performance at the maximum power point (MPP), when significant current flows in the device.

As shown earlier, a main loss mechanism in both cell architectures is the QFLS– $e$ ·V<sub>OC</sub> mismatch. While the potential V<sub>OC</sub> is higher for p–i–n as compared with n–i–p devices, the measured V<sub>OC</sub> is lower. The QFLS– $e$ ·V<sub>OC</sub> mismatch amounts to 68 meV for n–i–p and to 153 meV for p–i–n. To reveal the influence of the specific perovskite absorber composition and the interface formed to the respective CTLs, we compare p–i–n CsPbI<sub>2</sub>Br solar cells to organic–inorganic triple-cation (3Cat) perovskite solar cells. The 3Cat composition of Cs<sub>0.05</sub>(FA<sub>0.5</sub>MA<sub>0.5</sub>)<sub>0.95</sub>Pb(I<sub>0.5</sub>Br<sub>0.5</sub>)<sub>3</sub> was chosen here to have a reference solar cell with a similar bandgap and comparable transport layers as the CsPbI<sub>2</sub>Br solar cells. Figure S13, Supporting Information, shows the maxima of the first derivative  $\partial(EQE)/\partial\lambda$  of CsPbI<sub>2</sub>Br and 3Cat perovskite solar cells to prove that their bandgap is very similar.

The neat 3Cat film on glass yields a QFLS and PLQY of 1.363 eV and 0.0714%, respectively. This PLQY is higher than for MAPbI<sub>3</sub> films in our previous study but lower than the PLQY of 3Cat composition of lower bandgaps, which showed values close to 1%.<sup>[16]</sup> 3Cat solar cells were produced as described by Peña-Camargo et al.<sup>[28]</sup> and MeO-2PACz was replaced by 2PACz to avoid charge extraction issues.

Very interestingly, CsPbI<sub>2</sub>Br layer stacks show overall much larger QFLS than the layer stacks of the 3Cat, see **Figure 5a**. However, the final V<sub>OC</sub> of the best CsPbI<sub>2</sub>Br solar cell is much lower as compared with 3Cat devices, as shown in Figure 5c and Table S2, Supporting Information. The CsPbI<sub>2</sub>Br stack exhibits a



**Figure 5.** Comparison between p–i–n CsPbI<sub>2</sub>Br and triple-cation perovskite with similar band gap (Cs<sub>0.05</sub>(FA<sub>0.5</sub>MA<sub>0.5</sub>)<sub>0.95</sub>Pb(I<sub>0.5</sub>Br<sub>0.5</sub>)<sub>3</sub>). a) Mean QFLS values from two samples measured for different layer stacks and V<sub>OC</sub> of best solar cells. b) Bar chart displaying the origin of the voltage loss based on QFLS and V<sub>OC</sub> shown in panel (a). c) Reverse  $J$ – $V$  curves of CsPbI<sub>2</sub>Br and triple-cation perovskite solar cells.



QFLS of 1.39 eV and a final device  $V_{OC}$  of 1.21 V, while the 3Cat shows lower QFLS of only 1.29 eV, but a higher  $V_{OC}$  of 1.28 V. That sums up to a  $QFLS-e \cdot V_{OC}$  mismatch of only 10 meV being in line with well-optimized perovskite solar cells,<sup>[37]</sup> whereas the difference is more than 15 times larger for CsPbI<sub>2</sub>Br solar cells.

The main QFLS loss for 3Cat solar cells stems from the HTL/perovskite interface, as shown in Figure 5b. This has also been observed for double-cation perovskite solar cells with a bandgap of 1.7–1.8 eV using PTAA as HTL.<sup>[37]</sup> While the QFLS losses at the HTL/perovskite interface are much lower for CsPbI<sub>2</sub>Br than for 3Cat films, the losses at the perovskite/ETL interface are larger. This indicates potential differences in band alignment with the transport layers, which we investigate in the following section. The resulting reverse-scan  $J-V$  curves of CsPbI<sub>2</sub>Br and 3Cat solar cells are shown in Figure 5c. The  $J-V$  curves show almost the same  $J_{SC}$  and FF values but a higher  $V_{OC}$  for the 3Cat perovskite, resulting in a higher reverse-scan PCE of 15.8% compared with 14.67%.

### 3. Origin of $QFLS-e \cdot V_{OC}$ mismatch

As discussed in the introduction, the  $QFLS-e \cdot V_{OC}$  mismatch has mostly been attributed to three possible mechanisms or a combination of those: energy-level misalignment, poor charge selectivity, and a low-conductivity interlayer.

To investigate the energy-level alignment at the perovskite/ETL interface, we measured UPS and XPS on CsPbI<sub>2</sub>Br films with and without a 23 nm C<sub>60</sub> layer. The parameters obtained from the UPS data are shown in Table S3, Supporting Information, and the spectra are shown in Figure S14, Supporting Information. The valence band maximum (VBM) and highest occupied molecular orbital (HOMO) positions were extracted from the UPS data following the procedures as described in other studies.<sup>[38,39]</sup> The conduction band minimum (CBM) and lowest unoccupied molecular orbital (LUMO) position were then calculated using the optical bandgap of CsPbI<sub>2</sub>Br, see Figure S3, Supporting Information, and the electronic band gap of C<sub>60</sub> as given in the study by Akaike et al.<sup>[40]</sup>

Note that the work function, VBM, and HOMO have been measured on the surfaces of the respective materials.

The resulting energy-level diagram for CsPbI<sub>2</sub>Br is shown in Figure 6a. It reveals an energy offset between the perovskite CBM and the LUMO of the C<sub>60</sub>. This energy-level misalignment is responsible for the observed  $QFLS-e \cdot V_{OC}$  mismatch, as the band offset limits the  $V_{OC}$  of the CsPbI<sub>2</sub>Br solar cell, as shown in the study by Stolterfoht et al.<sup>[18]</sup> We note that at this point we do not exclude other contributions to the  $QFLS-e \cdot V_{OC}$  mismatch. Figure 6b shows the energy levels from measurements on a CsPbI<sub>2</sub>Br/1 nm LiF/23 nm C<sub>60</sub> stack. By adding the LiF interlayer between the perovskite and the C<sub>60</sub>, the C<sub>60</sub> LUMO is shifted upward, that is, away from the Fermi level. The vacuum level is also higher as compared with the CsPbI<sub>2</sub>Br/C<sub>60</sub> stack, but the difference between vacuum level and LUMO, that is, the electron affinity, is slightly reduced.

Figure 6c shows the energy levels of a 3Cat perovskite film with a bandgap of 1.88 eV. The parameters obtained from the UPS data are shown in Table S3, Supporting Information, and the spectra are shown in Figure S15, Supporting Information. Here, relative to the ITO Fermi level, 3Cat and C<sub>60</sub> show a higher CBM and LUMO than CsPbI<sub>2</sub>Br and C<sub>60</sub>. In addition, the offset between the perovskite and C<sub>60</sub> vacuum levels is smaller as compared with CsPbI<sub>2</sub>Br. The offset in the vacuum level gives rise to the built-in voltage of the junction, that is, the sum of the band bending in both perovskite and C<sub>60</sub> and of eventual dipoles.

To compare the band offsets between perovskite and C<sub>60</sub> in the three stacks, we use the Anderson rule. This rule states that the vacuum levels of two semiconductors forming a heterojunction should align.<sup>[41]</sup> The band offset at the perovskite/C<sub>60</sub> interface is then equal to the difference in electron affinity of the two materials. The resulting band offsets are 0.75 eV for CsPbI<sub>2</sub>Br/C<sub>60</sub>, 0.71 eV for CsPbI<sub>2</sub>Br/LiF/C<sub>60</sub>, and 0.57 eV for 3Cat/C<sub>60</sub>. This could explain why the  $QFLS-e \cdot V_{OC}$  mismatch is largest for solar cells with CsPbI<sub>2</sub>Br/C<sub>60</sub>, lower with CsPbI<sub>2</sub>Br/LiF/C<sub>60</sub> and lowest with 3Cat/LiF/C<sub>60</sub>. As we do not expect the presence of interface dipoles, we consider these values to be a good estimate of the

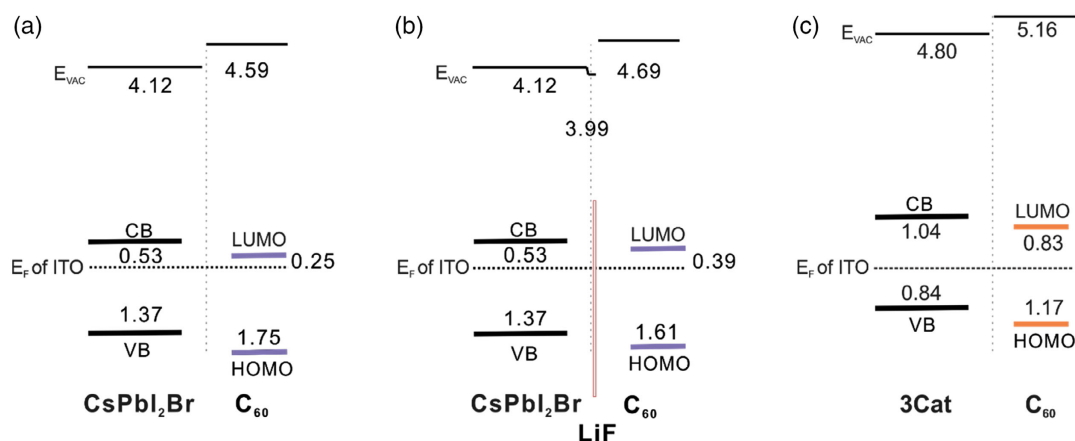


**Figure 6.** Energy-level diagram for a) CsPbI<sub>2</sub>Br, b) CsPbI<sub>2</sub>Br with 1 nm of LiF, and c) triple-cation perovskite, from UPS and XPS measurements on MeO-2PACz/perovskite films with and without 23 nm of C<sub>60</sub>. The measurements were conducted with reduced photon flux of the excitation source. All values shown in the energy-level diagram are in units of eV and refer to the Fermi level. The shown Fermi level is obtained by contacting the ITO substrate under the perovskite and is assumed to stay constant throughout the layer stack.

real band offsets at the interfaces that are caused by band bending. The calculated band offsets do not consider effects such as hybridization, introduction of interface states, or energy-level pinning. However, if such effects occur, they most likely occur in both CsPbI<sub>2</sub>Br and 3Cat samples. Therefore, we expect the trends in the band offset to be reliable.

The reduction of the band offset by the LiF interlayer is a possible explanation for the improved  $V_{OC}$  in solar cells with LiF as shown in Table 4: LiF had a similar effect for both CsPbI<sub>2</sub>Br and 3Cat solar cells, as solar cells with 3Cat/C<sub>60</sub> showed a QFLS- $e \cdot V_{OC}$  mismatch of 90 meV compared with 11 meV with 3Cat/LiF/C<sub>60</sub>. Solar cells with CsPbI<sub>2</sub>Br/C<sub>60</sub> showed a QFLS- $e \cdot V_{OC}$  mismatch of 272 meV compared with 179 meV with CsPbI<sub>2</sub>Br/LiF/C<sub>60</sub>. We note that there are generally at least two contributions giving rise to increased nonradiative recombination in the presence of a CTL, which is the energy-level offset and the interfacial defect density. While both effects lower the PLQY and thus the QFLS, the energy-level offset causes a further reduction of the  $V_{OC}$  to values below the QFLS. Here, the LiF interlayer substantially decreases the QFLS- $e \cdot V_{OC}$  mismatch of CsPbI<sub>2</sub>Br solar cells. This confirms that LiF improves the  $V_{OC}$  by reducing the energy level offset.

In conclusion, we show that energy-level misalignment between CsPbI<sub>2</sub>Br and C<sub>60</sub> contributes to the QFLS- $e \cdot V_{OC}$  mismatch and that a LiF interlayer decreases the misalignment and increases the device  $V_{OC}$ . How much of this QFLS- $e \cdot V_{OC}$  mismatch stems from low charge selectivity of the CTL and a low-mobility interlayer forming on the interface requires further investigation.

## 4. Conclusion

In this work, we investigated in detail the efficiency potential of CsPbI<sub>2</sub>Br films and solar cells by studying both material properties revealed by PL and solar cell characteristics. We showed that the fabrication method developed for this study yielded purely inorganic perovskite films with good morphology and pure  $\gamma$ -phase. We fabricated perovskite films on various CTLs to identify the most promising bottom CTL for p-i-n and n-i-p CsPbI<sub>2</sub>Br solar cells using intensity-dependent PL measurements. These measurements allowed us to construct potential  $J-V$  curves for films and stacks, revealing an efficiency potential of 21.6% for perovskite films on glass, 20.8% on compact TiO<sub>2</sub>, 20.5% on P3CT-N, and 20.3% on MeO-2PACz. The QFLS on MeO-2PACz is only 33 meV lower than on glass. On compact TiO<sub>2</sub> and P3CT-N, the QFLS is only 49 and 54 meV lower than on glass, respectively. This suggests a very low density of defects. For the first time, we demonstrated p-i-n CsPbI<sub>2</sub>Br solar cells using the HTL MeO-2PACz. On the best-performing solar cells, we performed a layer-by-layer loss analysis. This revealed that in the n-i-p CsPbI<sub>2</sub>Br solar cells, losses in QFLS are caused in almost equal parts by ETL and HTL, while in the p-i-n solar cells, the main part of the QFLS losses is caused by the ETL. As both configurations show a large QFLS- $e \cdot V_{OC}$  mismatch not observed in organic-inorganic solar cells, we further investigated the energy-level alignment using UPS and XPS measurements. We identified energy-level misalignment as a possible reason for the large QFLS- $e \cdot V_{OC}$  mismatch in p-i-n CsPbI<sub>2</sub>Br solar

cells. The negative effect of this energy-level misalignment is reduced by introducing a LiF interlayer between CsPbI<sub>2</sub>Br and C<sub>60</sub>, increasing the  $V_{OC}$  by 110 meV. On MeO-2PACz, the efficiency potential of CsPbI<sub>2</sub>Br is 20.3% with a  $pV_{OC}$  of 1.44 V. A more well-aligned ETL will push the PCE of p-i-n CsPbI<sub>2</sub>Br solar cells closer to this efficiency potential.

Overall, the voltage loss of inorganic perovskite solar cells is still higher than for organic-inorganic perovskites. We show that the  $V_{OC}$  is not limited by the inorganic composition, as the QFLS of a CsPbI<sub>2</sub>Br layer stack is higher as compared with an organic-inorganic perovskite with similar bandgap and CTLs. As we show here, intensity-dependent PL measurements create the opportunity to quickly compare the efficiency potential of perovskite with different CTLs without the need to fabricate and optimize full devices.

## Supporting Information

Supporting Information is available from the Wiley Online Library or from the author.

## Acknowledgements

We thank M. Gabernig, C. Ferber, T. Lußky, H. Heinz, C. Klimm, and M. Muske at Helmholtz-Zentrum Berlin (HZB) for technical assistance. We thank Florian Ruske for technical help with the SEM/EDS measurements. We thank P. Tockhorn for assistance with calculations with the transfer matrix method (TMM). M.G., P.C., S.A., and D.N. acknowledge funding from the Helmholtz Association via HI-SCORE (Helmholtz International Research School). F.P.C., D.N., M.S., F.S., N.K., and S.A. acknowledge funding from the Deutsche Forschungsgemeinschaft (DFG, German Research Foundation) within Projects SFB 951 (182087777) and SPP 2196 (SURPRISE 423749265 and HIPSTER 424709669). F.P.C., D.N., M.S., L.K., and S.A. further acknowledge financial support by the Federal Ministry for Economic Affairs and Energy within the framework of the 7th Energy Research Programme (P3T-HOPE, 03EE1017C and P3T, 03EE1017A) and HyPerCells, a joint graduate school of the Potsdam University and the Helmholtz-Zentrum Berlin. M.S. further acknowledges the Heisenberg program from the Deutsche Forschungsgemeinschaft (DFG, German Research Foundation) for funding within project number 498155101.

Open Access funding enabled and organized by Projekt DEAL.

## Conflict of Interest

The authors declare no conflict of interest.

## Data Availability Statement

The data that support the findings of this study are available in the supplementary material of this article.

## Keywords

CsPbI<sub>2</sub>Br, efficiency potentials, inorganic perovskites, photoluminescence, solar cells, voltage losses

Received: August 17, 2022

Published online: September 20, 2022

- [1] C. C. Stoumpos, C. D. Malliakas, M. G. Kanatzidis, *Inorg. Chem.* **2013**, *52*, 9019.
- [2] Q. Dong, Y. Fang, Y. Shao, P. Mulligan, J. Qiu, L. Cao, J. Huang, *Science* **2015**, *347*, 967.
- [3] M. J. P. Alcocer, T. Leijtens, L. M. Herz, A. Petrozza, H. J. Snaith, *Science* **2013**, *342*, 341.
- [4] E. L. Unger, L. Kegelmann, K. Suchan, D. Sörell, L. Korte, S. Albrecht, *J. Mater. Chem. A* **2017**, *5*, 11401.
- [5] NREL National Renewable Energy Laboratory, *Best Research-Cell Efficiency Chart* <https://www.nrel.gov/pv/cell-efficiency.html> (accessed: March 2022).
- [6] A. Al-Ashouri, E. Köhnen, B. Li, A. Magomedov, H. Hempel, P. Caprioglio, J. A. Márquez, A. B. M. Vilches, E. Kasparavicius, J. A. Smith, N. Phung, D. Menzel, M. Grischek, L. Kegelmann, D. Skroblin, C. Gollwitzer, T. Malinauskas, M. Jošt, G. Matič, B. Rech, R. Schlattmann, M. Topič, L. Korte, A. Abate, B. Stannowski, D. Neher, M. Stolterfoht, T. Unold, V. Getautis, S. Albrecht, *Science* **2020**, *370*, 1300.
- [7] E. Smecca, Y. Numata, I. Deretzis, G. Pellegrino, S. Boninelli, T. Miyasaka, A. La Magna, A. Alberti, *Phys. Chem. Chem. Phys.* **2016**, *18*, 13413.
- [8] R. Cheacharoen, N. Rolston, D. Harwood, K. A. Bush, R. H. Dauskardt, M. D. McGehee, *Energy Environ. Sci.* **2018**, *11*, 144.
- [9] A. F. Akbulatov, L. A. Frolova, N. N. Dremova, I. Zhidkov, V. M. Martynenko, S. A. Tsarev, S. Y. Luchkin, E. Z. Kurmaev, S. M. Aldoshin, K. J. Stevenson, P. A. Troshin, *J. Phys. Chem. Lett.* **2020**, *11*, 333.
- [10] S. Tan, B. Yu, Y. Cui, F. Meng, C. Huang, Y. Li, Z. Chen, H. Wu, J. Shi, Y. Luo, D. Li, Q. Meng, *Angew. Chem., Int. Ed.* **2022**, *61*, <https://doi.org/10.1002/anie.202201300>.
- [11] D. B. Straus, S. Guo, A. M. Abeykoon, R. J. Cava, *Adv. Mater.* **2020**, *32*, 2001069.
- [12] J. K. Nam, M. S. Jung, S. U. Chai, Y. J. Choi, D. Kim, J. H. Park, *J. Phys. Chem. Lett.* **2017**, *8*, 2936.
- [13] X. Liu, H. Lian, Z. Zhou, C. Zou, J. Xie, F. Zhang, H. Yuan, S. Yang, Y. Hou, H. G. Yang, *Adv. Energy Mater.* **2022**, *12*, 2103933.
- [14] C. Polyzoidis, K. Rogdakis, E. Kymakis, *Adv. Energy Mater.* **2021**, *11*, 2101854.
- [15] J. Hwang, R. R. Rao, L. Giordano, Y. Katayama, Y. Yu, Y. Shao-Horn, *Science* **2017**, *358*, 751.
- [16] M. Stolterfoht, M. Grischek, P. Caprioglio, C. M. Wolff, E. Gutierrez-Partida, F. Peña-Camargo, D. Rothhardt, S. Zhang, M. Raoufi, J. Wolansky, M. Abdi-Jalebi, S. D. Stranks, S. Albrecht, T. Kirchartz, D. Neher, *Adv. Mater.* **2020**, *32*, 2000080.
- [17] A. Onno, C. Chen, Z. C. Holman, in *Conf. Rec. IEEE Photovolt. Spec. Conf.*, Institute of Electrical and Electronics Engineers (IEEE), New York, NY, USA **2019**, pp. 2329–2333. <https://doi.org/10.1109/PVSC40753.2019.8980762>.
- [18] M. Stolterfoht, P. Caprioglio, C. M. Wolff, J. A. Márquez, J. Nordmann, S. Zhang, D. Rothhardt, U. Hö, Y. Amir, A. Redinger, L. Kegelmann, F. Zu, S. Albrecht, N. Koch, T. Kirchartz, M. Saliba, T. Unold, D. Neher, *Energy Environ. Sci.* **2019**, *12*, 2778.
- [19] P. Würfel, U. Würfel, *Physics of Solar Cells: From Basic Principles to Advanced Concepts*, 3rd ed., John Wiley & Sons, Hoboken, NJ, USA **2016**.
- [20] P. Caprioglio, M. Stolterfoht, C. M. Wolff, T. Unold, B. Rech, S. Albrecht, D. Neher, *Adv. Energy Mater.* **2019**, *9*, 1901631.
- [21] S. Ullah, J. Wang, P. Yang, L. Liu, Y. Li, S. E. Yang, T. Xia, H. Guo, Y. Chen, *Energy Technol.* **2021**, *9*, 2100691.
- [22] A. Magomedov, A. Al-Ashouri, E. Kasparavicius, S. Strazdaite, G. Niaura, M. Jošt, T. Malinauskas, S. Albrecht, V. Getautis, *Adv. Energy Mater.* **2018**, *8*, 1801892.
- [23] A. Al-Ashouri, E. Köhnen, B. Li, A. Magomedov, H. Hempel, P. Caprioglio, J. A. Márquez, A. B. Morales Vilches, E. Kasparavicius, J. A. Smith, N. Phung, D. Menzel, M. Grischek, L. Kegelmann, D. Skroblin, C. Gollwitzer, T. Malinauskas, M. Jošt, G. Matič, B. Rech, R. Schlattmann, M. Topič, L. Korte, A. Abate, B. Stannowski, D. Neher, M. Stolterfoht, T. Unold, V. Getautis, S. Albrecht, *Science* **2020**, *370*, 1300.
- [24] S. C. Liu, Z. Li, Y. Yang, X. Wang, Y. X. Chen, D. J. Xue, J. S. Hu, *J. Am. Chem. Soc.* **2019**, *141*, 18075.
- [25] V. Sarritzu, N. Sestu, D. Marongiu, X. Chang, S. Masi, A. Rizzo, S. Colella, F. Quochi, M. Saba, A. Mura, G. Bongiovanni, *Sci. Rep.* **2017**, *7*.
- [26] F. Lang, E. Köhnen, J. Warby, K. Xu, M. Grischek, P. Wagner, D. Neher, L. Korte, S. Albrecht, M. Stolterfoht, *ACS Energy Lett.* **2021**, *6*, 3982.
- [27] O. Almora, C. I. Cabrera, J. Garcia-Cerrillo, T. Kirchartz, U. Rau, C. J. Brabec, *Adv. Energy Mater.* **2021**, *11*, 2100022.
- [28] F. Peña-Camargo, P. Caprioglio, F. Zu, E. Gutierrez-Partida, C. M. Wolff, K. Brinkmann, S. Albrecht, T. Riedl, N. Koch, D. Neher, M. Stolterfoht, *ACS Energy Lett.* **2020**, *5*, 2728.
- [29] X. Li, Y. C. Wang, L. Zhu, W. Zhang, H. Q. Wang, J. Fang, *ACS Appl. Mater. Interfaces* **2017**, *9*, 31357.
- [30] M. Abdi-Jalebi, Z. Andaji-Garmaroudi, S. Cacovich, C. Stavrakas, B. Philippe, J. M. Richter, M. Alsari, E. P. Booker, E. M. Hutter, A. J. Pearson, S. Lilliu, T. J. Savenije, H. Rensmo, G. Divitini, C. Ducati, R. H. Friend, S. D. Stranks, *Nature* **2018**, *555*, 497.
- [31] M. Kim, G. H. Kim, T. K. Lee, I. W. Choi, H. W. Choi, Y. Jo, Y. J. Yoon, J. W. Kim, J. Lee, D. Huh, H. Lee, S. K. Kwak, J. Y. Kim, D. S. Kim, *Joule* **2019**, *3*, 2179.
- [32] F. Giordano, A. Abate, J. P. Correa Baena, M. Saliba, T. Matsui, S. H. Im, S. M. Zakeeruddin, M. K. Nazeeruddin, A. Hagfeldt, M. Graetzel, *Nat. Commun.* **2016**, *7*.
- [33] A. Marronnier, G. Roma, S. Boyer-Richard, L. Pedesseau, J. M. Jancu, Y. Bonnassieux, C. Katan, C. C. Stoumpos, M. G. Kanatzidis, J. Even, *ACS Nano* **2018**, *12*, 3477.
- [34] S. S. Mali, J. V. Patil, P. S. Shinde, G. de Miguel, C. K. Hong, *Matter* **2021**, *4*, 635.
- [35] K. Jiang, J. Wang, F. Wu, Q. Xue, Q. Yao, J. Zhang, Y. Chen, G. Zhang, Z. Zhu, H. Yan, L. Zhu, H. L. Yip, *Adv. Mater.* **2020**, *32*, 1908011.
- [36] J. Thiesbrummel, V. M. Le Corre, F. Peña-Camargo, L. Perdigon-Toro, F. Lang, F. Yang, M. Grischek, E. Gutierrez-Partida, J. Warby, M. D. Farrar, S. Mahesh, P. Caprioglio, S. Albrecht, D. Neher, H. J. Snaith, M. Stolterfoht, *Adv. Energy Mater.* **2021**, *11*, 2101447.
- [37] R. D. J. Oliver, P. Caprioglio, F. Peña-Camargo, L. R. V. Buizza, F. Zu, A. J. Ramadan, S. G. Motti, S. Mahesh, M. M. McCarthy, J. H. Warby, Y. H. Lin, N. Koch, S. Albrecht, L. M. Herz, M. B. Johnston, D. Neher, M. Stolterfoht, H. J. Snaith, *Energy Environ. Sci.* **2022**, *15*, 714.
- [38] J. Endres, D. A. Egger, M. Kulkarni, R. A. Kerner, L. Zhao, S. H. Silver, G. Hodes, B. P. Rand, D. Cahen, L. Kronik, A. Kahn, *J. Phys. Chem. Lett.* **2016**, *7*, 2722.
- [39] F. Zu, P. Amsalem, D. A. Egger, R. Wang, C. M. Wolff, H. Fang, M. A. Loi, D. Neher, L. Kronik, S. Duhm, N. Koch, *J. Phys. Chem. Lett.* **2019**, *10*, 601.
- [40] K. Akaike, K. Kanai, H. Yoshida, J. Tsutsumi, T. Nishi, N. Sato, Y. Ouchi, K. Seki, *J. Appl. Phys.* **2008**, *104*, 023710.
- [41] R. L. Anderson, *IBM J. Res. Dev.* **2010**, *4*, 283.
- [42] T. J. Jacobsson, A. Hultqvist, A. García-Fernández, A. Anand, A. Al-Ashouri, A. Hagfeldt, A. Crovetto, A. Abate, A. G. Ricciardulli, A. Vijayan, A. Kulkarni, A. Y. Anderson, B. P. Darwich, B. Yang, B. L. Coles, C. A. R. Perini, C. Rehermann, D. Ramirez, D. Fairén-

- Jimenez, D. Di Girolamo, D. Jia, E. Avila, E. J. Juarez-Perez, F. Baumann, F. Mathies, G. S. A. González, G. Boschloo, G. Nasti, G. Paramasivam, G. Martínez-Denegri, et al., *Nat. Energy* **2021**, *7*, 107.
- [43] J. Liang, P. Zhao, C. Wang, Y. Wang, Y. Hu, G. Zhu, L. Ma, J. Liu, Z. Jin, *J. Am. Chem. Soc.* **2017**, *139*, 14009.
- [44] W. Xiang, Z. Wang, D. J. Kubicki, X. Wang, W. Tress, J. Luo, J. Zhang, A. Hofstetter, L. Zhang, L. Emsley, M. Grätzel, A. Hagfeldt, *Nat. Commun.* **2019**, *10*.
- [45] X. Liu, H. Lian, Z. Zhou, C. Zou, J. Xie, F. Zhang, H. Yuan, S. Yang, Y. Hou, H. G. Yang, *Adv. Energy Mater.* **2022**, *12*, 2103933.
- [46] X. Gu, W. Xiang, Q. Tian, S. F. Liu, *Angew. Chem.* **2021**, *133*, 23348.